Research Square

Preprints are preliminary reports that have not undergone peer review.
They should not be considered conclusive, used to inform clinical practice,
or referenced by the media as validated information.

Influence of randomly distributed fractures on thermal extraction from a single-well enhanced geothermal system

Qiang Huang
University of Science and Technology of China
Jia-Hao Chen
University of Science and Technology of China
Hai-Bo Huang
University of Science and Technology of China
Mao-Bin Hu
humaobin@ustc.edu.cn

University of Science and Technology of China

Research Article

Keywords: Enhanced geothermal system, Discrete fracture network, Thermal energy extraction, Percolation

Posted Date: May 7th, 2026

DOI: https://doi.org/10.21203/rs.3.rs-9478532/v1

License: This work is licensed under a Creative Commons Attribution 4.0 International License.
Read Full License

Additional Declarations: No competing interests reported.

Influence of randomly distributed fractures on thermal extraction from a single-well enhanced geothermal system

Qiang Huang[1], Jia-Hao Chen[1], Hai-Bo Huang[1], Mao-Bin Hu[1,*]

[1] *School of Engineering Science, University of Science and Technology of China, Hefei, Anhui 230026, China;*

Abstract:

Enhanced geothermal systems (EGS) aim to efficiently explore the thermal resource of hot dry rock (HDR). A permeable fracture network is essential for the effective thermal extraction of EGS. In this paper, we developed a 3D discrete fracture network model and constructed a thermo-hydraulic-mechanical (THM) coupling model to investigate the impact of structural heterogeneity, including fracture intensity, length and orientation. The results indicate that under the same fracture intensity, when the proportion of longer fractures is higher and the fracture orientation is more random, the thermal extraction efficiency will be higher. The calculation of percolation probability of fracture networks further confirmed the permeability of the EGS increase with these structural factors. The results provide valuable insights for optimizing fracture network design in EGS.

Keywords: Enhanced geothermal system; Discrete fracture network; Thermal energy extraction; Percolation.

1. Introduction

Hot dry rock (HDR) is a high-temperature rock mass situated at depths of 3-10 kilometers [1]. HDR resources are geographically widespread, occurring in a variety of geological structures across the globe. As a clean and renewable energy source, given its substantial reserves, it is a geothermal energy resource with considerable potential for development. However, the low porosity (less than 5%) and low permeability (less than $10^{-15}m^2$) of HDR present significant challenges to the development and utilization of deep geothermal reservoirs. In order to extract heat from low-permeability HDR, it is necessary to construct an enhanced geothermal system (EGS) by creating high-permeability fracture networks through hydraulic stimulation and other means. The fracture network represents the primary conduit for fluid flow and heat transfer [2, 3]. Its geometric configuration and intrinsic characteristics exert a pronounced influence on the thermal exploitation of EGS. Understanding the effects of fracture parameters on EGS thermal extraction is essential for optimizing the process of fracturing, and increasing the EGS energy output to ensure long-term operational reliability.

Actual fracture networks are randomly distributed with different locations, lengths and orientations. These characteristics directly affect fluid flow and heat transfer. In previous researches, the equivalent continuum model [4-7] and discrete fracture network (DFN) model [8-12] were proposed to simulate fluid flow and heat transfer. The equivalent continuum model is suitable for reservoirs with dense and uniform fractures. However, when the fractures are unevenly distributed, ignoring the geometric details of the fractures will lead to large errors. In contrast, the DFN model clearly describes the shape, size, location and connectivity of fractures, so as to accurately simulate

* Corresponding Author. Email: humaobin@ustc.edu.cn

the process of fluid flow and heat transfer [12]. Using a two-dimensional (2D) DFN model, Zhang et al. found that there is a positive or negative correlation between the thermal performance of EGS and the geometric connectivity of fracture network [13]. Zhang et al. further studied the influence of fracture density on thermal recovery of five fracture parameters, and found that the increase of fracture density enhanced the flow and delayed the heat drop [14]. Zhou et al. showed that, compared with adding new fractures, expanding the aperture of existing fractures can effectively improve EGS performance [15].

While the DFN model excels in capturing fracture geometry and spatial distribution, its computational complexity poses a challenge. To address this issue, Fourno et al. developed the FraC mesh generation method, which constructs high-quality meshes in complex fracture networks [16]. Tene et al. introduced a projection technique to embed fractures into matrix grids, maintaining accuracy while significantly reducing computational cost [17]. Hyman et al. created an open-source software integrating fracture network generation, meshing, and flow/transport simulation, greatly advancing the application of DFN models [18].

Recently, three-dimensional (3D) DFN models have attracted much attention in EGS research [19]. 3D DFN models provide a more realistic representation of actual fracture networks, thus enabling more accurate modeling of fluid transport and heat transfer processes. For example, Zhan et al. used a 3D DFN model to analyze flow and transport in rough-walled fracture networks, showing that increased fracture roughness enhances local channel flow and accelerates transport processes [20]. Kang et al. simulated fluid transport under varying levels of pore size heterogeneity in a 3D DFN [21]. Yao et al. investigated the effects of fracture density and roughness on heat-flow coupling in 3D DFN [22].

Percolation theory, as a branch of statistical physics, provides a framework for understanding the connectivity and flow characteristics of complex networks [23]. Percolation theory can be used to analyze fracture networks in EGS. By determining the percolation threshold—the critical point at which the fracture network transitions from disconnected to connected—it helps to assess the minimum fracture density required for long-distance fluid flow [24]. This threshold is crucial for EGS because it defines the minimum requirement for establishing effective flow paths between injection and production wells.

Despite the advantages of DFN models in simulating the heterogeneity of fracture networks, uncertainties remain regarding which type of fracture network best enhances thermal extraction in single-well EGS configurations. Single-well EGS has gained increasing attention due to its lower cost and higher efficiency [25, 26]. Identifying key fracture parameters affecting single-well EGS thermal extraction are of great importance. Compared to traditional fracture models, 3D DFN models offer a superior framework for capturing the intricate interplay of fracture network structure and percolation dynamics. Detailed studies on the effect of heterogeneity of fracture network structure on single-well EGS thermal extraction are needed.

In this study, we evaluate the influence of randomly distributed fracture network on the flow and transport behavior in EGS. First, a 3D DFN was generated using a successive addition algorithm, and a thermo-hydraulic-mechanical (THM) coupling model was established to analyze the fluid flow and heat transfer process within the fractured rock masses. The influence of various network parameters on heat extraction was then statistically analyzed from the perspective of DFN percolation probability. The findings provide a valuable reference for the effective design and development of fractured EGS.

The remainder of this paper is organized as follows. Section 2 introduces the fracture network generation process and the governing equations of the THM model. Section 3 describes the model setup. Section 4 presents the detailed results and discussion. Finally, the main findings are summarized in Section 5.

2. Methodology

In this section, the generation method of 3D DFN is presented, and a numerical THM coupled model is proposed to simulate the fluid transport and heat transfer process in fractured reservoirs.

Fig. 1(a) shows a schematic diagram of single-well EGS. The EGS enables injection and extraction through casing single-well with two branch wells. As depicted in the figure, cool fluid is injected via the upper branch well with a flat horizontal fracture, then the hot fluid is extracted through the lower branch well with another horizontal fracture. The mass rock between the two branch wells is the reservoir, and has a 3D heterogeneous fracture structure. For simplicity, the reservoir is simulated as a cubic domain measuring 100×100×100m.

As shown in Fig. 1(b), a 3D DFN model is used to represent random fractures in the reservoir. Then a THM model is constructed to simulate the fluid transport and heat transfer process in the EGS.

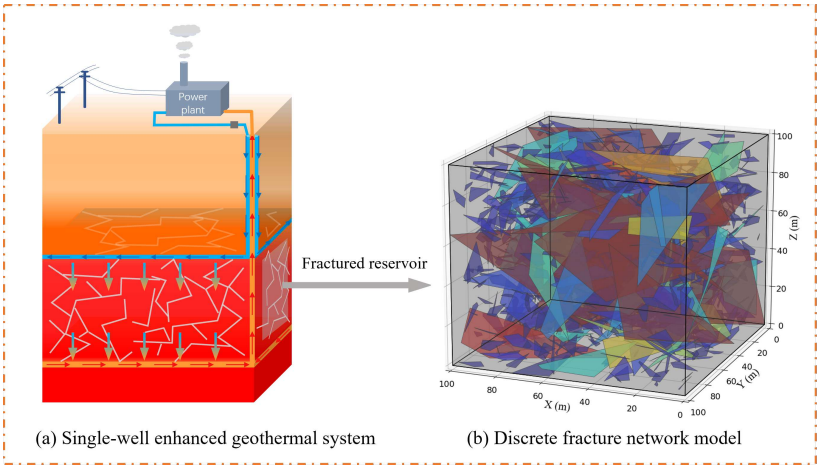


Fig. 1. Single-well EGS and fractured reservoir model.

2.1. 3D DFN model of the fractured reservoir

Fractured reservoir is located in the deep stratum, with complex fracture geometries. DFN model can generate fracture network according to probability distribution functions. As shown in Fig. 2(a), the studied reservoir is a cubic domain of size 100×100×100m, and the fractures are represented by convex quadrangles.

The 3D DFN model is generated based on the successive random addition algorithm. The geometrical parameters of each new fracture can be obtained by taking random values from predetermined probability distribution functions [27-29]. Geological studies indicate that the distribution of fracture lengths in many rock masses follows a power-law distribution [30-33], that is, small fractures are abundant, while large fractures are less common. In this study, the fracture length is sampled from a power-law distribution:

$$p(l) = dl^{-a}, \quad l \in [l_{\min}, l_{\max}] \tag{1}$$

where l is the fracture length; a is the power-law length exponent, which is ranged between 1 and

3; and d is the density term. The scale of the model domain L satisfied $l_{\min} \ll L \ll l_{\max}$, where $l_{\min}$ and $l_{\max}$ are the minimum and maximum fracture lengths. As shown in Fig. 2(c), power-law length exponent a is an important parameter of the distribution of fracture lengths. The choice of a directly influences the connectivity of the fracture network by controlling the proportion of short and long fractures, thereby affecting the overall network connectivity. When a is small, the proportion of long fractures increases, potentially enhancing network connectivity. Conversely, when a is large, short fractures dominate, reducing connectivity and possibly restricting fluid flow.

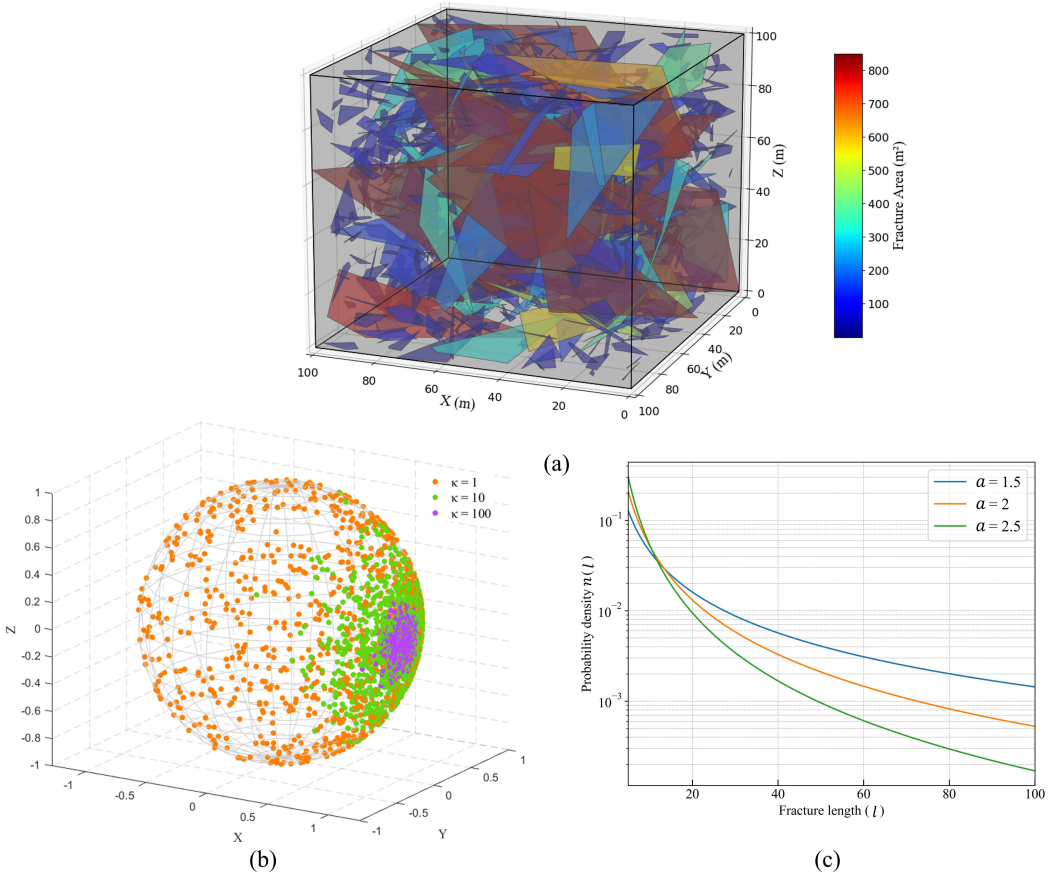


Fig. 2. (a) DFN model; (b) Schematic diagram of fracture direction distribution on a von Mises-Fisher unit sphere, with a mean direction of (1,0,0), where κ controls the concentration of the distribution; (c) The probability density function of power-law length distribution with different exponent a.

The orientation vector of the fracture is determined by the von Mises-Fisher distribution, which is defined on the n-dimensional unit sphere. If a random n dimensional unit vector $\vec{x}$ obeys von Mises-Fisher distribution, its probability distribution function is defined as [34]:

$$f(\vec{x}|\vec{\mu},\kappa) = C_n(\kappa)\exp(\kappa\vec{\mu}^T\vec{x}) \tag{2}$$

where $C_n(\kappa)$ is

$$C_n(\kappa) = \frac{\kappa^{\frac{n}{2}-1}}{(2\pi)^{\frac{n}{2}} I_{\frac{n}{2}-1}(\kappa)} \tag{3}$$

where $\vec{\mu}$ is the unit vector denoting the mean direction of the distribution; $\kappa \geq 0$ is the concentration parameter, the larger the value, the more the data are concentrated in the mean direction, and when κ=0, the distribution degenerates to a uniform distribution; $I_v(\kappa)$ denotes the

modified Bessel function of the first kind. Fig. 2(b) shows the schematic diagram of von Mises-Fisher distribution of different parameter κ values on the unit sphere (n=3). The choice of the concentration parameter κ determines the dispersion of fracture orientations. In actual geological formations, the dispersion of fracture orientations is influenced by geological structures and stress fields. For example, in regions dominated by a single directional stress, fracture orientations are more concentrated, requiring a larger κ value. In contrast, in structurally complex areas, fracture orientations are more dispersed, necessitating a smaller κ value. Thus, the selection of κ corresponds to the geological background of different target reservoirs, enabling the model to better reflect the actual distribution characteristics of fracture orientations.

Finally, the fracture intensity ρ is calculated as the total fracture surface area per unit volume [35]:

$$\rho = \frac{\sum_i S_i}{L^3} \tag{4}$$

where S_i is the surface area of the ith fracture; and L^3 is the total volume of the domain.

2.2. Thermal-hydraulic-mechanical coupling model

2.2.1. Model assumptions

From the above description, the fractured geothermal reservoir is considered as a dual medium consisting of rock matrix and DFN. The following assumptions were made in developing the mathematical model of the fractured reservoir:

(1) The reservoir consists of a fracture network and a rock matrix. The rock matrix can be described as an isotropic and homogeneous porous medium and the deformation follows a linear elastic model. This assumption is applicable when the physical properties of the rock matrix (such as porosity, permeability, and elastic modulus) exhibit minimal spatial variation. The linear elastic model can adequately simulate rock behavior under conditions of small stress and deformation.

(2) The working fluid is water, which is considered as a single-phase fluid, no phase transition occurs in the simulation process. The fluid flow follows Darcy's law [36-39]. In single-phase flow, Darcy's law accurately describes the movement of the fluid in porous media, making this simplification suitable for many conventional geothermal system simulations.

(3) Heat exchange obeys Fourier's law. The heat exchange between the reservoir and the fracture network is realized by heat conduction and heat convection [14, 40, 41], which can be described by local heat equilibrium. This assumption is suitable for scenarios where the heat exchange process is relatively stable, simplifying the thermodynamic calculations.

(4) There is no thermal compensation around the reservoir surface, and the in-situ stress in rock matrix is not considered. The rock deformation takes into account thermal expansion and internal stresses induced by pore pressure. In local geothermal development simulations, the impact of surrounding thermal compensation and in-situ stress is minimal, making this assumption reasonable.

(5) No new fractures will be generated during the simulation process. Under conditions of low injection pressure or minimal thermal stress changes during the thermal extraction phase, the reservoir structure remains stable, and this assumption simplifies the simulation process.

In natural geothermal reservoirs, fracture surface roughness increases flow resistance, and fracture fillings (such as those from mineral dissolution-precipitation reactions) can partially or fully block flow paths, both of which reduce the effective permeability of fractures. This study focuses on flow and heat transfer behavior at the macro fracture network scale. To reduce computational

complexity, the model simplifies fluid transport at the micro fracture scale by neglecting the detailed effects of fracture surface roughness and fillings. In fact, using Eq. (16), the permeability of fractures can describe the overall flow resistance. This assumption may overestimate fluid flow rates through fractures but does not affect the flow and heat transfer behavior at the macro fracture network scale. These simplifying assumptions make the model computationally feasible and capable of adequately reflecting the characteristics of geothermal reservoirs under specific conditions.

Based on the above assumptions, the control equations for the thermo-hydraulic-mechanical (THM) coupling model can be derived.

2.2.2. Mass conservation equation

Fluid flow in the reservoir can be obtained by solving the mass conservation equations in the rock matrix and fractures, respectively.

The governing equation of fluid flow in rock matrix can be expressed by mass conservation equation as follows [42-44]:

$$S_m \frac{\partial p}{\partial t} + \nabla u_m + Q_m = 0 \tag{5}$$

where S_m denotes the water storage coefficient in rock matrix, $1/Pa$; p denotes the hydraulic pressure, Pa; t is the time of simulation, s; ∇ represents the spatial gradient operator; u_m denotes the flow velocity in the rock matrix, m/s; Q_m is the fluid source and sink term in the rock matrix, $kg/(m^3 \cdot s)$. According to the assumptions, the flow velocity of the fluid can be described by Darcy's law:

$$u_m = -\frac{\kappa_m}{\eta}\left(\nabla p + \rho_f g \nabla z\right) \tag{6}$$

where κ_m denotes the permeability of the rock matrix, m^2; η denotes the dynamic viscosity of the fluid, $Pa \cdot s$; ρ_f indicates the density of the fluid, kg/m^3; g is the gravitational acceleration, m/s^2.

The governing equation of fluid flow in the fracture is similar to that of the rock matrix, and the continuity equation in fractures can be described as [42-44]:

$$d_f S_f \frac{\partial p}{\partial t} + \nabla_\tau\left(d_f u_f\right) + Q_f = 0 \tag{7}$$

where u_f denotes flow velocity in the fracture, m/s; S_f denotes the specific storage of the facture, $1/Pa$; Q_f denotes the source and sink term on the fracture plane, m/s; ∇_τ denotes the gradient operator restricted to the fracture's tangential plane. According to the assumptions, the water flow in the fracture is also subject to Darcy's law, the water flow velocity is:

$$u_f = -\frac{\kappa_f}{\eta}\left(\nabla_\tau p + \rho_f g \nabla_\tau z\right) \tag{8}$$

where d_f denotes the aperture of the fracture, m; and κ_f denotes the permeability of the fractures.

The dynamic viscosity of water is affected by temperature [45], $\eta = \nu\rho_f$ in which ν is the kinematic viscosity of water. The commonly used empirical formula for kinematic viscosity is [46, 47]:

$$\nu = \frac{1.775}{1 + 0.0337T_f + 0.000221T_f^2} \tag{9}$$

In this work, the dynamic viscosity of water is described by the following empirical formula [48]:

$$\eta(T_f)=\begin{cases}1.38-0.0212T_f+1.3605\times10^{-4}T_f^2-4.6454\times10^{-7}T_f^3\\+8.9043\times10^{-10}T_f^4-9.0791\times10^{-13}T_f^5+3.8457\times10^{-16}T_f^6,\\273.15K\le T_f\le 413.15K\\0.004-2.1075\times10^{-5}T_f+3.8578\times10^{-8}T_f^2-2.3973\times10^{-11}T_f^3,\\413.15K\le T_f\le 553.15K\end{cases} \tag{10}$$

where T_f is the fluid temperature.

2.2.3. Energy conservation equation

In geothermal reservoirs, the transfer of heat is achieved by heat conduction and heat convection. Heat transfer process in the reservoir can be obtained by solving the energy conservation equation in the rock matrix and fractures, respectively.

According to the assumptions, the assumption of local thermal equilibrium is introduced to simplify the calculation. It is assumed that the thermophysical properties of the rock matrix, fractures and fluids in a computational cell can be expressed by effective values. The effective heat capacity and effective thermal conductivity are weighted averages of the water and rock matrix values [49, 50]:

$$\left(\rho C_p\right)_{\text{eff}}=\varphi\left(\rho_f C_f\right)+(1-\varphi)(\rho_m C_m) \tag{11}$$

$$\lambda_{\text{eff}}=\varphi\lambda_f+(1-\varphi)\lambda_m \tag{12}$$

where $\left(\rho C_p\right)_{\text{eff}}$ denotes the effective heat capacity; λ_{eff} denotes the effective thermal conductivity, $W/(m\cdot K)$; φ denotes porosity; C_f and C_m denote the heat capacity of water and rock matrix respectively, $J/(kg\cdot K)$; ρ_f and ρ_m denote the density of water and rock matrix respectively, kg/m^3; λ_f and λ_m denote the thermal conductivity of water and rock matrix respectively, $W/(m\cdot K)$.

According to the energy conservation theorem and the local thermal equilibrium theory, the governing equation of the temperature field in the rock matrix can be described as [49, 50]:

$$\left(\rho C_p\right)_{\text{eff}}\frac{\partial T}{\partial t}+\rho_f C_f u_m\nabla T-\nabla\cdot(\lambda_{\text{eff}}\nabla T)+q_{h,m}=0 \tag{13}$$

The governing equation of temperature field in the fracture is similar to that of rock matrix, and the energy conservation equation of the fracture can be described as [49, 50]:

$$d_f\left(\rho C_p\right)_{\text{eff}}\frac{\partial T}{\partial t}+d_f\rho_f C_f u_f\nabla T-\nabla\cdot\left(d_f\lambda_{\text{eff}}\nabla T\right)+q_{h,f}=0 \tag{14}$$

where $q_{h,m}$ is heat source and sink in the rock matrix, W/m^3; $q_{h,f}$ is heat source and sink in the fracture, W/m^2; T is the temperature, K; u is the flow velocity, m/s. The subscripts 'm' and 'f' represent rock matrix and fracture, respectively.

2.2.4. Stress balance equation

The equation of the linear elastic model can be described by Hooke's law as follows [51]:

$$\frac{3(1-v)}{1+v}\nabla^2\sigma_{total}+\frac{2(1-2v)}{1+v}\alpha_B\nabla^2 p+\frac{2(1-2v)}{1+v}K\alpha_T\nabla^2 T+\nabla\cdot\mathrm{G}=0 \tag{15}$$

where v is Poisson's ratio, σ_{total} is the mean total stress, G denotes the body force, α_B is the Biot's constants, α_T is the thermal expansion coefficient and K is the bulk module for rock matrix.

The mechanical processes in EGS will cause the permeability of pores and fractures in rock matrix to change with stress and strain. In this work, the porosity of the fracture is considered as a constant, and the permeability of the fracture can be expressed as [52]:

$$\kappa_f = \kappa_{f0}\, exp\left[-\left(\frac{\sigma_n'}{\gamma}\right)\right] \qquad (16)$$
$$\sigma_n' = \sigma_n - \alpha_B p$$

where κ_{f0} is initial permeability, σ_n' and σ_n are effective normal stress and total normal stress of fractures, respectively; γ is set as 20 MPa.

2.3. Model verification

The numerical simulation of fractured reservoir involves the physical process of fluid transport, heat transfer and reservoir deformation coupling. The accuracy of the numerical simulation is essential for the evaluation of the heat recovery system. Here the model is verified from the perspective of thermo-hydraulic (TH) coupling and thermal-hydraulic-mechanical (THM) coupling [53], and the commercial software COMSOL is used to solve the coupling model.

For the heat transfer in the fracture, a single fracture model is employed to verify the accuracy and reliability of the TH coupling model by comparing the numerical results with the analytical solution. The analytical solution proposed by Lauwerier et al. [54] and Barends et al. [55] describes the temperature variation within a single fracture. The schematic diagram of the single fracture model is shown in Fig. 3. There is a rock matrix area of $100\times100m$ and a horizontal fracture is located in the middle of the matrix. In the derivation of the analytical solution, it is assumed that the model extends infinitely along the x and y directions. The initial temperature of the heat source is constant. A fluid of constant temperature is injected at a constant rate from the left side of the fracture. The fracture aperture remains constant, and the rock matrix is assumed to be homogeneous and isotropic. Under the above assumptions, the analytical solution can be obtained as follows [49, 54, 55]:

$$T = T_0 + (T_{in} - T_0)\,\mathrm{erfc}\left(\frac{\lambda_m x}{\rho_f c_f d_f}\sqrt{\frac{\rho_m c_m}{u_f \lambda_m (u_f t - x)}}\right) U\left(t - \frac{x}{u_f}\right) \qquad (17)$$

where T_0 denote the initial temperature; T_{in} denotes the injection temperature; d_f is the fracture aperture; erfc is the complementary error function and U is the unit step function; λ denotes the thermal conductivity; ρ is the density; c is the heat capacity; u is the flow velocity. The subscripts 'm' and 'f' represent rock matrix and fracture, respectively.

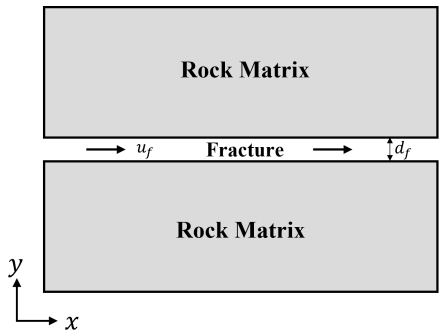


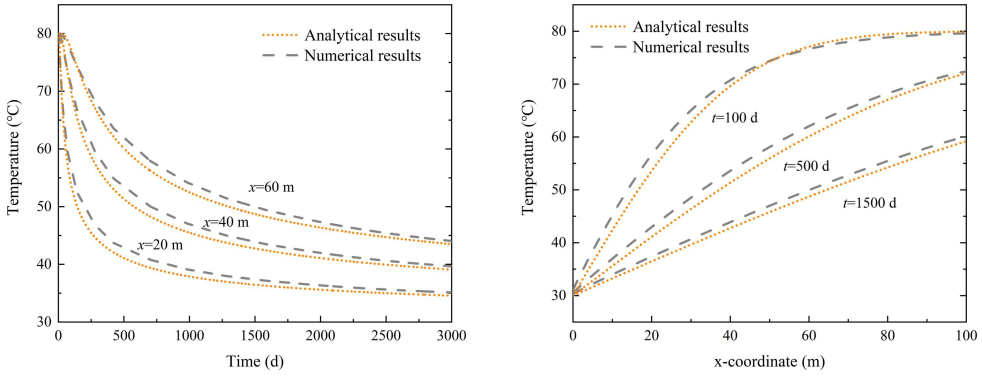
Fig. 3. Schematic diagram of single fracture model.

The left side of fracture is treated as the inlet and the right side as the outlet. Water is used as working fluid. The initial temperature is set to 80°C, and the inlet temperature and velocity are fixed as 30°C and $0.01m/s$, respectively. In addition, the outlet boundary is set to free flow. The detailed parameters for the analytical solution and the numerical simulation are listed in Table 1. The total

simulation period is 3000 days, and each time step is 1 day. Fig. 4 shows the comparison of analytical and numerical solutions. Fig. 4(a) describes the variation of temperature at different locations (x=20m, x=40m and x=60m) in the fracture. Fig. 4(b) shows the temperature distribution in the fracture at different time steps (t=100 d, t=500 d and t=1500 d). It can be seen that the numerical solution is in good accordance with the analytical one, demonstrating the accuracy of the numerical model. The slight discrepancy observed may be attributed to the fact that the analytical solution assumes an infinitely extended geometric region in the x and y directions, whereas the numerical model considers a finite region. Additionally, errors in mesh generation and discretization during the numerical simulation could also contribute to deviations in the results.

Table 1 Parameters for TH model validation [14, 39, 40, 56, 57]

Parameters	Unit	Value
Rock density ρ_m	kg/m^3	2700
Rock heat capacity c_m	J/(kg · K)	1000
Rock heat conductivity λ_m	W/(m · K)	2.8
Water density ρ_f	kg/m^3	1000
Water heat capacity c_f	J/(kg · K)	4200
Water viscosity η	Pa · s	0.001
Fracture aperture d_f	m	0.001
Flow velocity u_f	m/s	0.01
Initial temperature T_0	℃	80
Injection temperature T_{in}	℃	30



(a) Temperature distribution in the fracture at the locations of x=20 m, 40 m and 60 m

(b) Temperature distribution in the fracture at the times of t=100 d, 500 d and 1500 d

Fig. 4. Comparison of analytical and numerical solutions for temperature in a single fracture.

To verify the accuracy of THM coupling method, a linear elastic column model is used, as shown in Fig. 5. The 1D thermal consolidation of a linear elastic solid column under the condition of constant surface compression and constant surface temperature involves the mechanical deformation, temperature variation and pore pressure dissipation of saturated porous media, which is a typical THM coupling process. Bai et al. deduced the analytical solution of the 1D thermal consolidation problem to describe the changes of temperature, pore pressure and displacement [58].

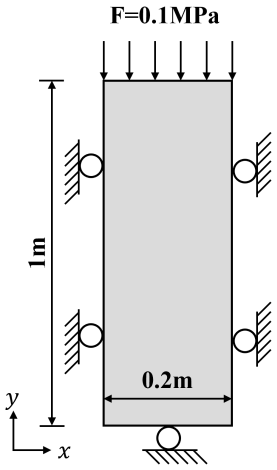


Fig. 5. Schematic diagram of linear elastic column model.

In the numerical process, the initial temperature is 283.15 K and the pore pressure is 0.1 MPa. The upper boundary temperature and hydraulic conditions are fixed at 333.15 K and 0 MPa, respectively. In addition, the top boundary is also subjected to an external pressure of 0.1 MPa. Other boundaries are set as adiabatic, no flow and zero displacement. The material parameters used in the numerical model are listed in Table 2. The results of THM coupling analysis are plotted in Fig. 6 which respectively show the variation of displacement, pore pressure and temperature at different positions (y=0.1m, y=0.6m, y=0.8m) in the soil column. Compared with the analytical solution of Bai, it can be seen that the numerical results are in good agreement with the analytical results, which verifies the accuracy of the THM coupling model.

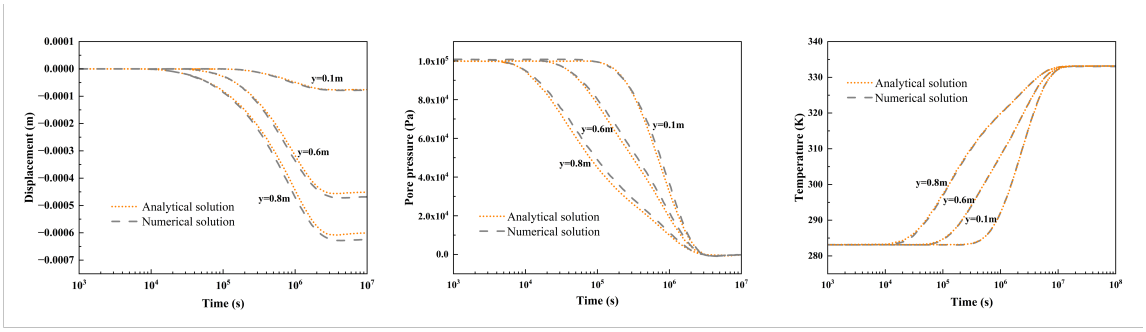


Fig. 6. The verification of THM coupling model.

Table 2 Parameters for THM model validation [53, 59].

Parameters	Value
Bulk modulus of solid	2×10^{10} Pa
Bulk modulus of water	5×10^{9} Pa
Elastic modulus	60 MPa
Biot coefficient	1
Poisson ratio	0.4
Thermal expansion coefficient	3×10^{-7} 1/K
Porosity	0.4
Solid heat conductivity	0.5 W/K/m
Solid heat capacity	800 J/kg/K

3. Model setup

3.1. Numerical model design and boundary conditions

The highly heterogeneous and anisotropic structure of the fracture network has a significant effect on the heat extraction performance of fractured reservoirs. This study explores the effect of heterogeneity of fracture structure on heat extraction from EGS, focusing on three critical fracture network parameters: the power-law length exponent a, the concentration parameter κ and the fracture intensity ρ. Fracture networks with different structures are generated by adjusting the generation parameters, with fracture sizes sampled from power-law distributions with exponents a, fracture orientations sampled from fisher distributions with concentration parameters κ. We set κ =0.1 to indicate that the fracture orientation obeys a random distribution. With different combinations of parameters, 12 distinct fracture network sets were created, with detailed settings outlined in Table 3. To reduce the effects of randomness in network generation, results for each parameter set are averaged over 10 independent simulations.

Table 3 Parameters for generating 3D DFNs in the present study.

Set	Fracture size: Power-law distribution	Fracture orientation: von Mises-Fisher distribution	Fracture intensity (m^{-1})
	a	κ	ρ
1	1.5		
2	2.0	0.1	0.06
3	2.5		
4	1.5		
5	2.0	0.1	0.10
6	2.5		
7	1.5		
8	2.0	0.1	0.14
9	2.5		
10		3	
11	2.0	5	0.10
12		7	

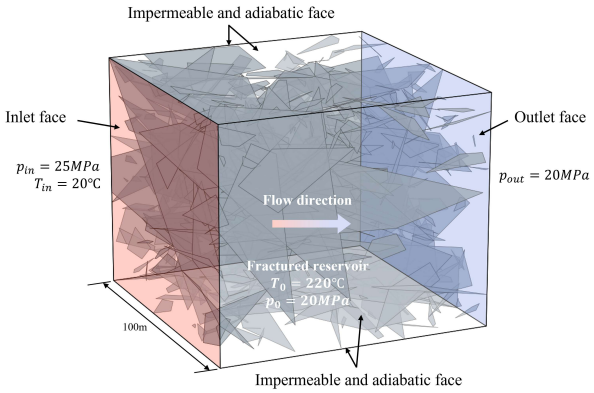


Fig. 7. Schematic diagram of initial and boundary conditions for discrete fracture network model

The numerical model represents a fractured reservoir as a cubic domain measuring $100\times100\times100m$. Fig. 7 provides a schematic of the initial and boundary conditions. For fluid flow, the boundary at x=0 serves as the water inlet, x=100 as the water outlet, and all other surfaces are impermeable and adiabatic. For the mechanical field, all external boundaries are fixed in the normal direction. Due to the low permeability of granite, the rock matrix permeability is set to $1\times10^{-18}\ m^2$ and the elastic modulus is set to 2.5×10^{10} Pa [14]. Parameters such as initial fracture permeability and fracture aperture are assigned values based on typical hydraulically conductive fractures in fractured reservoirs [40, 56, 57, 59, 60]. The key parameters governing the simulations are summarized in Table 4, ensuring a comprehensive setup for analyzing heat extraction in the fractured system.

Table 4 Parameters for the simulations[14, 40, 56, 57, 59, 60].

Parameters	Unit	Value
Rock density ρ_m	kg/m^3	2700
Rock heat capacity c_m	$J/(kg\cdot K)$	1000
Elastic modulus	Pa	2.5×10^{10}
Poisson ratio v		0.25
Biot-Wills coefficient α_B		1
Thermal expansion coefficient α_T	$1/K$	5×10^{-6}
Rock porosity		1%
Rock heat conductivity λ_m	$W/(m\cdot K)$	3.0
Rock permeability κ_m	m^2	1×10^{-18}
Rock specific storage S_m	$1/Pa$	1×10^{-8}
Water density ρ_f	kg/m^3	1000
Water heat capacity c_f	$J/(kg\cdot K)$	4200
Fracture aperture d_f	m	0.001
Fracture specific storage S_f	$1/Pa$	1×10^{-9}
Fracture porosity		99%
Fracture initial permeability κ_{f0}	m^2	1×10^{-11}
Inlet temperature T_{in}	K	293.15
Inlet pressure p_{in}	MPa	25
Outlet pressure p_{out}	MPa	20
Initial temperature T_0	K	493.15
Initial pressure p_0	MPa	20

3.2. Definition of assessment parameters

In order to evaluate the production performance of different EGSs, the appropriate evaluation parameters need to be defined.

The average temperature of the outlet can be calculated by the following equation:

$$T_{out}(t)=\frac{\int_\gamma u_f d_f T_f d\gamma+\iint_\Omega uT d\Omega}{\int_\gamma u_f d_f d\gamma+\iint_\Omega u d\Omega} \tag{18}$$

The average flow rate of the outlet can be calculated by the following equation:

$$Q(t) = \int_{\gamma} u_f d_f d\gamma + \iint_{\Omega} u d\Omega \tag{19}$$

The outlet average thermal power P can be calculated by the following equation:

$$P(t) = c_f Q(T_{out} - T_{in}) \tag{20}$$

where c_f is the heat capacity of water, T_{in} is temperature of the injected fluid.

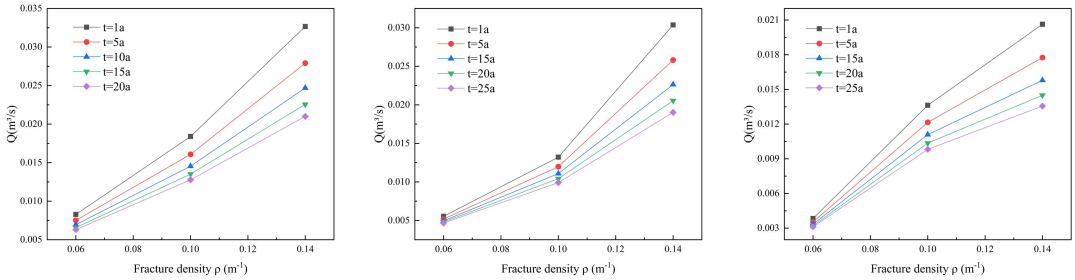
4. Results and discussion

4.1. Effect of fracture intensity and fracture length on thermal exploitation

This subsection discusses the effect of variations in fracture length and fracture intensity on thermal exploitation of fractured reservoirs, assuming a random orientation distribution of fractures. We investigate three power-law length exponent scenarios: a=1.5, 2.0 and 2.5, and three fracture intensity cases: ρ=0.06, 0.10 and 0.14m^{-1}. As detailed in Table 3, the fracture parameter settings for set 1 to 9 represent different combinations of these parameters. When a=1.5, the system is dominated by large fractures with high connectivity. When a=2.5, the system is dominated by small fractures with low connectivity. When ρ=0.06m^{-1}, the fractures in the system are sparse. When ρ=0.14m^{-1}, the fractures in the system are dense.

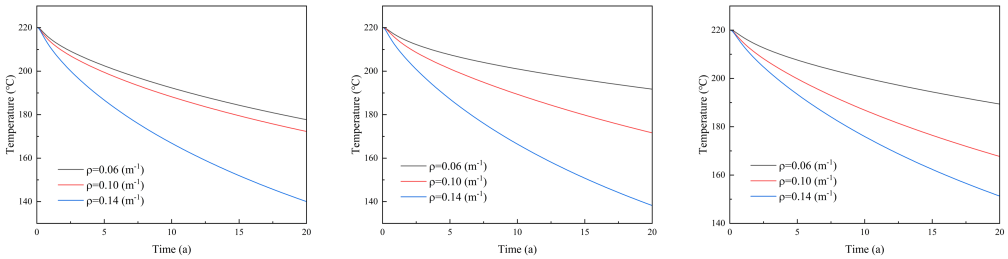
Fig. 8 illustrates the variation of outlet flow rate for different fracture intensities. The result shows that the outlet flow rate increases with fracture intensity across all years and for all three a values. With the passing of time, the outlet flow rate Q decreases. Moreover, the DFN of a=1.5 (Fig. 8(a)) exhibits a much higher outlet flow rate than the DFN of a=2.5 (Fig. 8(c)). The trend in the reservoir's outlet flow rate is caused by the interaction between fracture length distribution (controlled by a) and fracture intensity ρ. When a=1.5 and 2.0, the number of large fractures in the system increases significantly with increasing fracture intensity, leading to a substantial enhancement in the connectivity of the fracture system. Conversely, when a=2.5, the increase in the number of large fractures with increasing fracture intensity is less pronounced; at a fracture intensity of ρ=0.10m^{-1}, the system already forms a well-connected network, and although the addition of a few large fractures aids flow, the effect of connectivity has a reduced gain for the flow rate, leading to a convex trend in outlet flow rate.

Fig. 9 shows the variation of outlet temperature for different fracture intensities. When the fracture intensity is high (ρ=0.14m^{-1}), the flow rate of the fractured reservoir is the highest and the outlet temperature is the lowest due to rapid heat extraction. When the fracture intensity is low (ρ=0.06m^{-1}), the flow rate of the fractured reservoir is the minimum and the outlet temperature is the highest. Over time, thermal mining causes both outlet temperature and flow rate to decline. This behavior arises because higher fracture intensity increases the number of flow pathways, enhancing fluid circulation and convective heat transfer from the rock matrix to the fluid. Conversely, lower ρ restricts fluid movement, limiting convective heat exchange and preserving higher outlet temperatures longer. For lower a (e.g., 1.5), longer fractures create well-connected channels, boosting flow rates and accelerating heat extraction, which is more efficient but depletes thermal reserves faster.



(a) $a = 1.5$ (b) $a = 2.0$ (c) $a = 2.5$

Fig. 8. Variation of outlet flow rate Q for different fracture intensities at (a) $a = 1.5$, (b) $a = 2.0$ and (c) $a = 2.5$.



(a) $a = 1.5$ (b) $a = 2.0$ (c) $a = 2.5$

Fig. 9. Variation of outlet temperature for different fracture intensities at (a) $a = 1.5$, (b) $a = 2.0$ and (c) $a = 2.5$.

Fig. 10 presents the variation of outlet temperature and outlet flow rate for different power-law length exponents. In fig. 10(a) ρ=0.06m^{-1}, (b) ρ=0.10m^{-1} and (c) ρ=0.14m^{-1}, the outlet temperature shows lower sensitivity to the power-law length exponent a compared to the fracture intensity ρ, suggesting that fracture intensity plays a more dominant role in controlling temperature dynamics. Fig. 10(d) illustrates the variation of outlet flow rate for different power-law length exponents and fracture intensities in different time, using the same dataset as Fig. 8 but analyzed from the perspective of the power-law length exponent, thus the flow rate variation in Fig. 10(d) exhibits trends similar to those in Fig. 8. Therefore, the system's outlet flow rate shows a convex trend at a fracture intensity of ρ=0.14m^{-1}, while it displays a concave trend at fracture intensities of ρ=0.06 and 0.10m^{-1}. Additionally, as the power-law length exponent a increases from 1.5 to 2.5, the proportion of smaller fractures rises, reducing network connectivity and causing the flow rate to decrease; conversely, the flow rate increases with higher fracture intensity ρ.

Fig. 11 further demonstrates that average outlet power is significantly influenced by ρ: at ρ=0.14m^{-1}, the power output is highest but declines rapidly over time, while at ρ=0.06m^{-1}, the power output is lowest and remains more stable. Across all ρ values, power is maximized at a=1.5 and minimized at a=2.5.

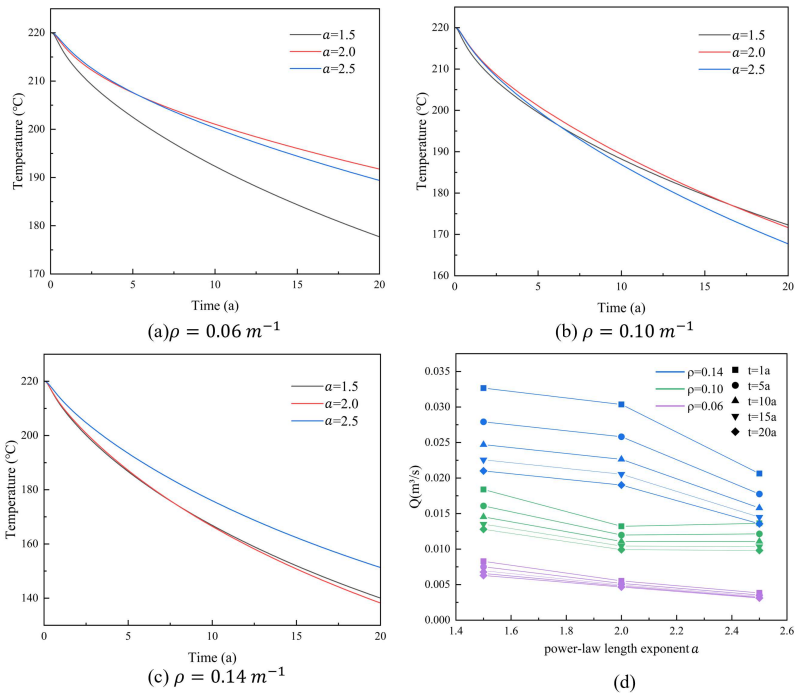


Fig. 10. Variation of outlet temperature for different power-law length exponents at (a) ρ=0.06m^{-1}, (b) ρ=0.10m^{-1} and (c) ρ=0.14m^{-1}; (d) Variation of outlet flow rate Q for different power-law length exponents and fracture intensities in different time (1, 5, 10, 15, 20 years).

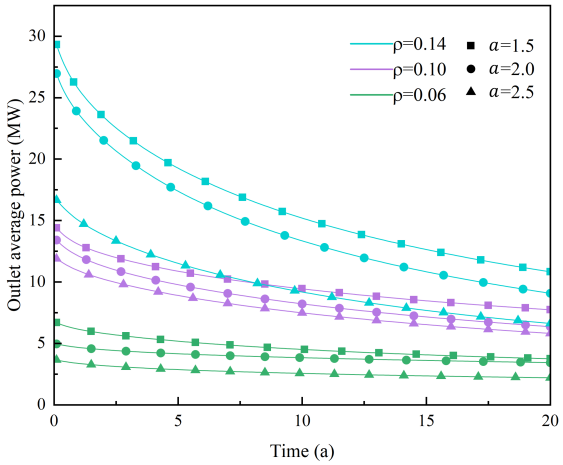


Fig. 11. Variation of outlet average power for different power-law length exponents and fracture intensities.

Fig. 12 shows the schematic diagram of the isothermal surface of the fractured reservoir under different parameters ρ and α. It can be clearly seen that the larger the fracture intensity ρ is, the more uniform the distribution of the low temperature region in the reservoir, and the best heat recovery effect is achieved when ρ=0.14. Additionally, higher ρ increases fracture surface area available for heat exchange, enhancing conductive transfer from the matrix to fractures, while lower α amplifies this by forming extensive flow paths that improve both convection and overall thermal extraction efficiency.

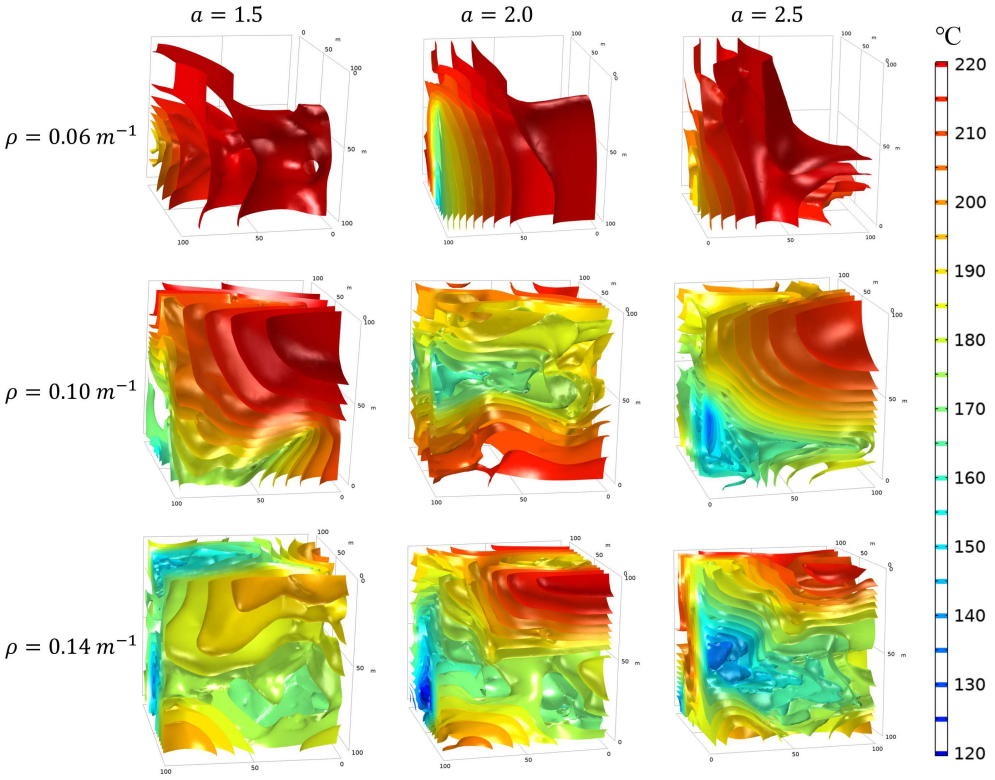


Fig. 12. Schematic temperature distribution of reservoir isothermal surfaces at different power-law length exponents and fracture intensities in the 10th year (The first model of each set was shown; The left surface is the entrance surface; isothermal surfaces at 5°C intervals from 120 to 220°C).

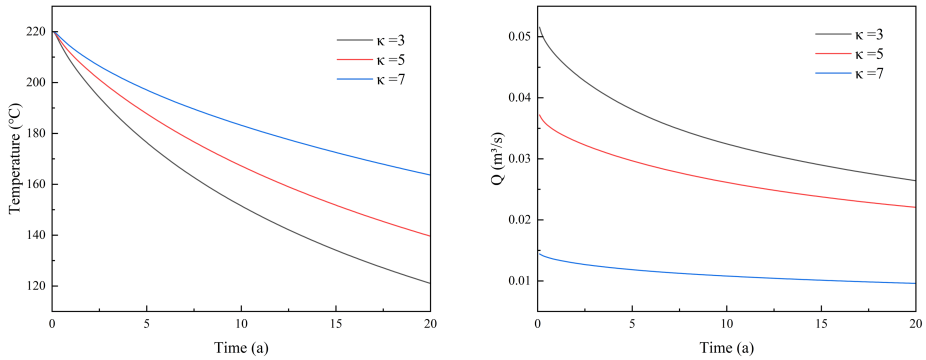
From an EGS engineering perspective, high ρ (e.g., $0.14m^{-1}$) and low a (e.g., 1.5) optimize short-term heat extraction by maximizing flow and power output, ideal for projects prioritizing rapid energy yield, such as peak-load power generation. Low ρ (e.g., $0.06m^{-1}$) and high a (e.g., 2.5) suit long-term, stable output scenarios. Yao et al. [22] and Zhang et al. [61] observed in their fracture network studies that increasing fracture density significantly improves reservoir heat extraction efficiency. Zhang et al. [13] further showed that a higher proportion of longer fractures in the system enhances the geometric connectivity of the fracture network. Our findings agree with their conclusions. Moreover, compared to these studies, our 3D DFN model and percolation probability analysis provide deeper insights into how structural heterogeneity affects thermal efficiency.

From the above analysis, fracture intensity ρ emerges as a key indicator of reservoir connectivity. Increasing ρ adds more fractures, fostering better connectivity and optimizing thermal recovery. A lower a increases large fractures, enhancing network connectivity, while ρ primarily drives flow rate and power output. A combination of high ρ and low a yields superior connectivity, favoring thermal exploitation. Overall, parameter ρ exerts a stronger influence on connectivity than parameter a.

4.2. Effect of fracture orientation on thermal exploitation

This subsection discusses the effect of fracture orientation on thermal exploitation of fractured reservoirs. Here the fracture intensity ρ is set to $0.10m^{-1}$, the power-law length exponent a is set to 2.0. Three different cases of Fisher distribution concentration parameters are analyzed: κ=3, 5

and 7. As shown in Table 3, the fracture parameter settings for set 10 to 12 show three different combinations of concentration parameter κ. The mean direction of the distribution is set to (1, 0, 0), and the concentration of the fracture orientation is controlled by changing the concentration parameter κ. A larger κ indicates that fracture orientations are more concentrated around the mean direction, reducing randomness, while a smaller κ results in more randomly oriented fractures, enhancing the potential for interconnection.



(a) (b)

Fig. 13. Variation of outlet temperature and flow rate Q under different concentration parameters.

Fig. 13 shows the variation of outlet temperature and flow rate under different concentration parameters. With an increase in κ, the outlet temperature rises, and the outlet flow rate decreases. When κ=3, the reservoir outlet temperature is the lowest, the outlet flow rate is the highest, and the heat extraction effect is the most efficient. Conversely, when κ=7, the reservoir outlet temperature is the highest, the outlet flow is the lowest, and the heat extraction effect is the least efficient. This trend arises because a lower κ (e.g., 3) leads to more randomly oriented fractures, increasing the likelihood of fracture intersections and forming a well-connected network that enhances fluid circulation and convective heat transfer. In contrast, a higher κ (e.g., 7) results in more aligned fractures, reducing the number of intersecting pathways and limiting fluid flow, which restricts heat exchange between the rock matrix and the fluid.

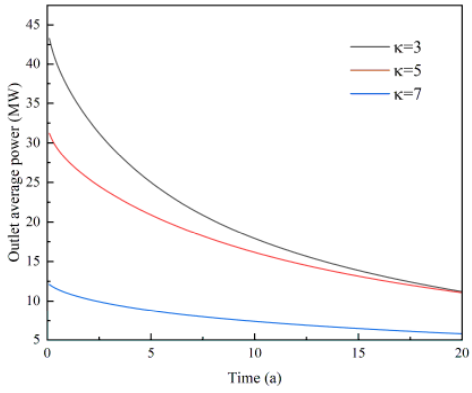


Fig. 14. Variation of outlet average power under different concentration parameters.

Fig. 14 shows the variation of average outlet power under different concentration parameters. The highest outlet average power is achieved at κ=3, and the lowest outlet average power is achieved at κ=7. The variation in κ directly alters the connectivity of the reservoir, as confirmed by the percolation probability analysis in Section 4.3 (Fig. 15(b)). At ρ=0.10m^{-1}, Fig. 15(b)

indicates that the percolation probability (P) is highest at κ=3, approaching 0.9, and lowest at κ=7, where (P) is nearly 0. This high percolation probability at κ=3 reflects a more connected network, facilitating greater fluid flow and heat extraction, as evidenced by the higher outlet flow rate and power output in Figs. 13 and 14. Conversely, the low percolation probability at κ=7 corresponds to reduced connectivity, leading to lower flow rates and power outputs, which aligns with the observed decline in thermal extraction efficiency.

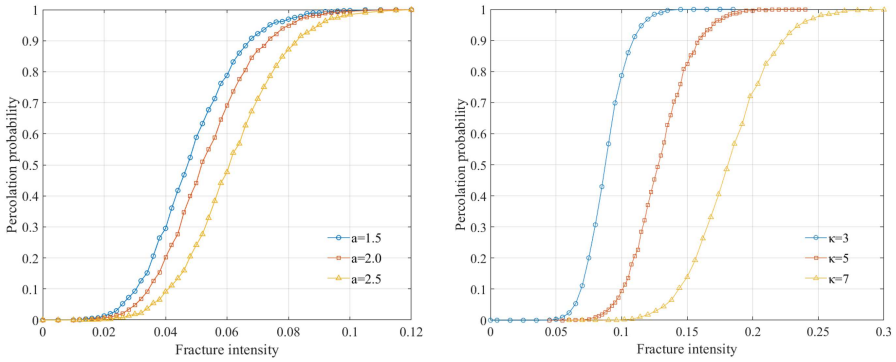
4.3. Percolation probability of fracture network

In a finite field, the percolation phenomenon of fracture network refers to the seepage channel where the fractures intersect to form a breakthrough [62]. The increase in fracture intensity causes fractures interconnected to form a complete seepage flow through the rock mass. In this section, we investigate the effect of fracture parameters on the percolation probability of DFN through Monte Carlo tests. The seepage/percolation probability is defined as follows:

$$\mathrm{P} = \frac{N_{per}}{N_{sum}} \tag{21}$$

where N_{per} is the number of percolated fracture networks, and N_{sum} is total number of fracture networks.

We set the parameters as: a=1.5, 2.0, 2.5 and κ=3, 5, 7, respectively. Under different fracture intensities, 10000 DFN samples are randomly generated for each set of parameters, and the connectivity of each sample is checked to obtain the percolation probability (P) using Eq. (21).



(a) (b)

Fig. 15. Variation of percolation probability of different DFN parameters under different fracture intensity. (a) Percolation probability with different size exponent a; (b) Percolation probability with different orientation concentration parameter κ.

Fig. 15 illustrates the variation of percolation probability under different fracture network parameters with different fracture intensity. For all subfigures, the percolation probability increases with the intensity of fracture. With the same fracture intensity, Fig. 15(a) shows that the percolation probability in the DFN is highest at a=1.5, indicating that more large fractures will promote the formation of percolated DFN. Similarly, Fig. 15(b) reveals that the smaller κ (more random orientation of fractures) favor the development of a percolated DFN. The results agree to and explain well the previous phenomena of thermal extraction. These trends in percolation probability directly correlate with the thermal extraction efficiency observed in Sections 4.1 and 4.2. For instance, in Section 4.1 (Figs. 8 and 11), the highest outlet flow rate and power output were observed at a=1.5 and ρ=0.14m^{-1}, conditions under which Fig. 15(a) shows a percolation probability reaches 1 when

ρ=0.12m^{-1}, reflecting a highly connected network that enhances fluid circulation and convective heat transfer. Conversely, at a=2.5 and lower ρ (e.g., 0.06m^{-1}), the percolation probability is significantly lower, corresponding to the reduced flow rates and slower heat extraction seen in Section 4.1 due to limited connectivity. Similarly, Section 4.2 (Figs. 13 and 14) demonstrates that a lower κ=3 yields the highest flow rate and best heat extraction, consistent with Fig. 15(b), where κ=3 results in the highest percolation probability at the same fracture intensity, facilitating better network connectivity and fluid flow.

To further elucidate the effects of parameters a, κ, and ρ on percolation probability, Fig. 16 presents contour maps and 3D surface plots of percolation probability under different parameters. Under different parameters, the percolation probability increases with increasing fracture intensity. The contour map in Fig. 16(a) describes the relationship between percolation probability (P) and fracture intensity ρ (0.02 to 0.12m^{-1}) and power-law length exponent a (1.5 to 2.5) for a fixed κ=0.1, showing yellow regions where percolation is most likely to occur. For instance, at a=1.5 and ρ> 0.05m^{-1}, (P) exceeds 0.5, indicating a critical threshold for achieving connectivity of fracture network. Under the same fracture intensity, the variation in percolation probability with different values of exponent a is relatively small, indicating that the exponent a has a minor influence on the percolation probability of the fracture network, and as exponent a increases, the percolation probability gradually decreases, leading to reduced system connectivity. This corresponds to the thermal extraction performance of the fracture system in Section 4.1 (Figs. 10 and 11), where the influence of exponent a on thermal extraction performance is minor, and the system's thermal extraction performance decreases as exponent a increases.

Similarly, Fig. 16(b) shows a contour map of the relationship between (P) and ρ (0.05 to 0.25m^{-1}) and concentration parameter κ (3 to 7) for a fixed exponent a=2.0, revealing that (P) approaches 1 at κ=3 and ρ> 0.12m^{-1}, highlighting the role of random orientations in enhancing connectivity. Under the same fracture intensity, the variation in percolation probability with different values of κ is significant. For example, at ρ=0.12m^{-1}, the percolation probability at κ=3 is close to 0.9; while at κ=7, it is close to 0. This phenomenon indicates that the parameter κ has a substantial impact on the percolation probability of the fracture network. As κ increases, the percolation probability decreases rapidly. This corresponds to the thermal extraction performance of the fracture system in Section 4.2 (Figs. 13 and 14), where the influence of κ on thermal extraction performance is significant, and the system's thermal extraction performance declines rapidly as κ increases.

The 3D surface plot in Fig. 16(c) visualizes (P) for varying ρ and a, showing that at lower values of exponent a, (P) increases more rapidly, and the difference in percolation probability between different values of exponent a is relatively small. Fig. 16(d) shows (P) for varying ρ and κ. It can be seen that, lower value of κ leads to a faster rise in (P), and the difference in percolation probability between different values of κ is significant. These phenomena underscore the importance of large fractures (low a) and random orientations (low κ) in forming a percolated network, aligning with the thermal extraction results in Section 4.1 and 4.2, where optimal heat recovery was achieved at a=1.5, κ=3, and ρ=0.14m^{-1}, conditions corresponding to high (P) regions in Fig. 16.

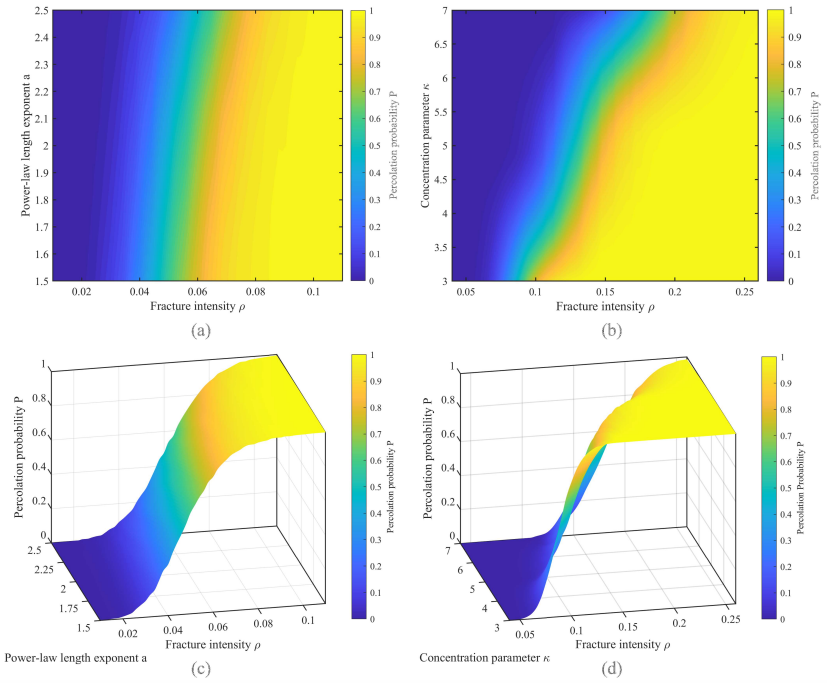


Fig. 16. Contour map and 3D surface of percolation probability under different parameters

Importantly, regions with high percolation probability (e.g., P > 0.9) exhibit significantly enhanced thermal extraction efficiency. For example, at ρ=0.14m^{-1}, a=1.5, and κ=3, the percolation probability P approaches 1.0, leading to a highly connected network that maximizes fluid circulation and heat transfer, as evidenced by the superior thermal performance observed in Sections 4.1 and 4.2.

From an EGS engineering perspective, these findings offer practical guidance for reservoir design and stimulation strategies. A high percolation probability is essential for efficient fluid circulation and heat extraction in EGS systems. For example, targeting a fracture network with large and dense fractures (low a and high ρ) and random orientations (low κ) can maximize connectivity and thermal recovery. In EGS engineering, hydraulic fracturing can be tailored to promote the formation of large fractures (low a) and random orientations (low κ), potentially through controlled injection pressures and multi-stage fracturing techniques.

5. Conclusion

In summary, this paper investigates the influence of randomly distributed fracture network on the thermal extraction of a single-well EGS. First, a 3D discrete fracture network (DFN) model is developed using the successive random addition algorithm. Next, a thermal-hydraulic-mechanical (THM) coupled model is constructed to simulate the fluid flow and heat transfer process in the reservoir. We investigate the DFN with different sets of fracture parameters, and analyze the effects of structural heterogeneity (such as fracture intensity, fracture length and fracture orientation) on heat extraction from the EGS. The impact of fracture parameters on the percolation probability of reservoir was also investigated.

This study contributes to EGS research by the use of 3D DFN model, while THM model enables a comprehensive simulation of reservoir thermal extraction behavior. The incorporation of percolation probability analysis also offers a quantitative tool to predict and optimize heat extraction.

Based on the obtained results, the following conclusions can be drawn.

(1) Fracture intensity plays a key role in enhancing EGS thermal performance. Higher fracture intensity improves fracture connectivity, leading to increased outlet temperature, outlet flowrate and outlet power.

(2) With the same fracture intensity, fracture networks with more larger fractures perform better compared to those dominated by smaller fractures, due to enhanced connectivity and increased flow pathways, as evidenced by higher outlet flow rates and lower outlet temperatures.

(3) Increasing the randomness of fracture orientations enhances heat extraction by improving fracture network connectivity, while highly aligned fractures reduce flow pathways and efficiency.

(4) The percolation probability of reservoir increases with the fracture intensity and is higher in fracture networks with more large fractures and more random orientations. Regions with high percolation probability demonstrate significantly better thermal extraction performance.

These findings provide valuable practical applications for the design and operation of EGS. From an EGS engineering perspective, a high fracture intensity ρ with long fractures optimize short-term heat extraction by maximizing flow rates and power output, making them ideal for projects prioritizing rapid energy yield. Conversely, a low fracture intensity ρ with short fractures are better suited for long-term, stable output scenarios, ensuring sustained performance over extended periods. Additionally, when optimizing fracture network, one should aim for a fracture network with high randomness in orientation, as this enhances connectivity and facilitates efficient heat extraction.

Acknowledgement

The research was supported by the Key Research and Development Program of China (No. 2021YFB150740502).

References

[1] Tester, J.W., B.J. Anderson, A.S. Batchelor, D.D. Blackwell, R. DiPippo, E.M. Drake, J. Garnish, B. Livesay, M. Moore, and K. Nichols, *The future of geothermal energy.* Massachusetts Institute of Technology, 2006. **358**: p. 1-3.

[2] Sudicky, E.A. and E.O. Frind, *Contaminant Transport in Fractured Porous-Media - Analytical Solutions for a System of Parallel Fractures.* Water Resources Research, 1982. **18**(6): p. 1634-1642.

[3] Tang, D., E. Frind, and E.A. Sudicky, *Contaminant transport in fractured porous media: Analytical solution for a single fracture.* Water resources research, 1981. **17**(3): p. 555-564.

[4] Warren, J.E. and P.J. Root, *The behavior of naturally fractured reservoirs.* Society of Petroleum Engineers Journal, 1963. **3**(03): p. 245-255.

[5] Tsang, Y.W., C.F. Tsang, F.V. Hale, and B. Dverstorp, *Tracer transport in a stochastic continuum model of fractured media.* Water Resources Research, 1996. **32**(10): p. 3077-3092.

[6] Barenblatt, G., Y.P. Zheltov, and I. Kochina, *Basic concepts in the theory of seepage of homogeneous liquids in fissured rocks.* Journal of Applied Mathematics and Mechanics, 1960. **24**(5): p. 852-864.

[7] Jackson, C.P., A.R. Hoch, and S. Todman, *Self-consistency of a heterogeneous continuum porous medium representation of a fractured medium.* Water Resources Research, 2000. **36**(1):

p. 189-202.

[8] Barenblatt, G.I., I.P. Zheltov, and I. Kochina, *Basic concepts in the theory of seepage of homogeneous liquids in fissured rocks [strata].* Journal of applied mathematics and mechanics, 1960. **24**(5): p. 1286-1303.

[9] Dverstorp, B. and J. Andersson, *Application of the discrete fracture network concept with field data: Possibilities of model calibration and validation.* Water Resources Research, 1989. **25**(3): p. 540-550.

[10] Cacas, M.-C., E. Ledoux, G. de Marsily, B. Tillie, A. Barbreau, E. Durand, B. Feuga, and P. Peaudecerf, *Modeling fracture flow with a stochastic discrete fracture network: calibration and validation: 1. The flow model.* Water Resources Research, 1990. **26**(3): p. 479-489.

[11] Zhou, D., A. Tatomir, H. Gao, Q. Liu, and M. Sauter, *Influences of directional aperture heterogeneity on the performances of two-phase enhanced geothermal system considering the CO2 buoyant force.* International Journal of Heat and Mass Transfer, 2024. **228**: p. 125611.

[12] Shi, J., L. Cheng, X. Rao, R. Cao, and G. Liu, *A modified embedded discrete-fracture model to study oil-water two-phase heat and mass transfer in the complex fracture network.* International Journal of Heat and Mass Transfer, 2021. **175**: p. 121215.

[13] Zhang, X., Z.Q. Huang, Q.H. Lei, J. Yao, L. Gong, and W.D. Yang, *Improving heat extraction performance of enhanced geothermal systems: Insights from critical fracture network parameter and multi-objective optimization method.* Applied Thermal Engineering, 2022. **213**: p. 118671.

[14] Zhang, W., Z.Q. Qu, T.K. Guo, and Z.Y. Wang, *Study of the enhanced geothermal system (EGS) heat mining from variably fractured hot dry rock under thermal stress.* Renewable Energy, 2019. **143**: p. 855-871.

[15] Zhou, D.J., A. Tatomir, A. Niemi, C.F. Tsang, and M. Sauter, *Study on the influence of randomly distributed fracture aperture in a fracture network on heat production from an enhanced geothermal system (EGS).* Energy, 2022. **250**: p. 123781.

[16] Fourno, A., T.-D. Ngo, B. Noetinger, and C. La Borderie, *FraC: A new conforming mesh method for discrete fracture networks.* Journal of Computational Physics, 2019. **376**: p. 713-732.

[17] Ţene, M., S.B. Bosma, M.S. Al Kobaisi, and H. Hajibeygi, *Projection-based embedded discrete fracture model (pEDFM).* Advances in Water Resources, 2017. **105**: p. 205-216.

[18] Hyman, J.D., S. Karra, N. Makedonska, C.W. Gable, S.L. Painter, and H.S. Viswanathan, *dfnWorks: A discrete fracture network framework for modeling subsurface flow and transport.* Computers & Geosciences, 2015. **84**: p. 10-19.

[19] Zhang, Q., A.D. Taleghani, and G. Li, *Fracture conductivity management to improve heat extraction in enhanced geothermal systems.* International Journal of Heat and Mass Transfer, 2024. **218**: p. 124725.

[20] Zhan, L., Y. Hu, L. Zou, W. Xu, Z. Ye, R. Chen, D. Zhuang, J. Li, and Y. Chen, *Effects of multiscale heterogeneity on transport in three-dimensional fractured porous rock with a rough-walled fracture network.* Computers and Geotechnics, 2022. **148**: p. 104836.

[21] Kang, P.K., J.D. Hyman, W.S. Han, and M. Dentz, *Anomalous transport in three-dimensional discrete fracture networks: Interplay between aperture heterogeneity and injection modes.* Water Resources Research, 2020. **56**(11): p. e2020WR027378.

[22] Yao, C., Y. Shao, J. Yang, F. Huang, C. He, Q. Jiang, and C. Zhou, *Effects of fracture density,*

roughness, and percolation of fracture network on heat-flow coupling in hot rock masses with embedded three-dimensional fracture network. Geothermics, 2020. **87**: p. 101846.

[23] Stauffer, D. and A. Aharony, *Introduction to percolation theory*. 2018: Taylor & Francis.

[24] Sahimi, M., *Applications of percolation theory*. 1994: CRC Press.

[25] Li, Z., J. Guo, W. Huang, J. Chen, K. Liu, J. Cen, Q. Ma, A. Li, B. Wang, and F. Jiang, *Heat extraction performance of the super-long gravity heat pipe applied to geothermal reservoirs of multi-aquifers.* International Journal of Heat and Mass Transfer, 2024. **225**: p. 125440.

[26] Wang, G., X. Song, G. Song, Y. Shi, C. Yu, F. Xu, J. Ji, and Z. Song, *Analyzes of thermal characteristics of a hydrothermal coaxial closed-loop geothermal system in a horizontal well.* International Journal of Heat and Mass Transfer, 2021. **180**: p. 121755.

[27] Fox, A., P. La Pointe, A. Simeonov, J. Hermanson, and J. Oehman, *Statistical geological discrete fracture network model. Forsmark modelling stage 2.2.* Sweden: N. p., 2007. SKB-R-07-46.

[28] Rouleau, A. and J.E. Gale, *Statistical Characterization of the Fracture System in the Stripa Granite, Sweden.* International Journal of Rock Mechanics and Mining Sciences, 1985. **22**(6): p. 353-367.

[29] Berkowitz, B., *Characterizing flow and transport in fractured geological media: A review.* Advances in Water Resources, 2002. **25**(8-12): p. 861-884.

[30] Dershowitz, W., P. Lapointe, and T. Cladouhos, *Derivation of fracture spatial pattern parameters from borehole data.* International Journal of Rock Mechanics and Mining Sciences, 1998. **35**(4): p. 508-508.

[31] Maffucci, R., S. Bigi, S. Corrado, A. Chiodi, L. Di Paolo, G. Giordano, and C. Invernizzi, *Quality assessment of reservoirs by means of outcrop data and "discrete fracture network" models: The case history of Rosario de La Frontera (NW Argentina) geothermal system.* Tectonophysics, 2015. **647**: p. 112-131.

[32] Nadimi, S., B. Forbes, J. Moore, R. Podgorney, and J. McLennan, *Utah FORGE: Hydrogeothermal modeling of a granitic based discrete fracture network.* Geothermics, 2020. **87**: p. 101853.

[33] Bour, O. and P. Davy, *Connectivity of random fault networks following a power law fault length distribution.* Water Resources Research, 1997. **33**(7): p. 1567-1583.

[34] Wood, A.T., *Simulation of the von Mises Fisher distribution.* Communications in statistics-simulation and computation, 1994. **23**(1): p. 157-164.

[35] Dershowitz, W.S. and H.H. Herda. *Interpretation of fracture spacing and intensity*. in *ARMA US rock mechanics/geomechanics symposium*. The 33rd U.S. Symposium on Rock Mechanics (USRMS), 1992. ARMA-92-0757.

[36] Baria, R., J. Baumgartner, F. Rummel, R.J. Pine, and Y. Sato, *HDR/HWR reservoirs: concepts, understanding and creation.* Geothermics, 1999. **28**(4-5): p. 533-552.

[37] Jiang, F.M., J.L. Chen, W.B. Huang, and L. Luo, *A three-dimensional transient model for EGS subsurface thermo-hydraulic process.* Energy, 2014. **72**: p. 300-310.

[38] Cheng, Q.L., X.N. Wang, and A. Ghassemi, *Numerical simulation of reservoir stimulation with reference to the Newberry EGS.* Geothermics, 2019. **77**: p. 327-343.

[39] Sun, Z.X., X. Zhang, Y. Xu, J. Yao, H.X. Wang, S.H. Lv, Z.L. Sun, Y. Huang, M.Y. Cai, and X.X. Huang, *Numerical simulation of the heat extraction in EGS with thermal-hydraulic-mechanical coupling method based on discrete fractures model.* Energy, 2017. **120**: p. 20-33.

[40] Gong, F.C., T.K. Guo, W. Sun, Z.M. Li, B. Yang, Y.M. Chen, and Z.Q. Qu, *Evaluation of geothermal energy extraction in Enhanced Geothermal System (EGS) with multiple fracturing horizontal wells (MFHW).* Renewable Energy, 2020. **151**: p. 1339-1351.

[41] Yao, J., X. Zhang, Z.X. Sun, Z.Q. Huang, J.R. Liu, Y. Li, Y. Xin, X. Yan, and W.Z. Liu, *Numerical simulation of the heat extraction in 3D-EGS with thermal hydraulic-mechanical coupling method based on discrete fractures model.* Geothermics, 2018. **74**: p. 19-34.

[42] Chen, B., E. Song, and X. Cheng. *Plane-symmetrical simulation of flow and heat transport in fractured geological media: A discrete fracture model with comsol*. Springer Series in Geomechanics and Geoengineering, 2013. **3**: p. 149-154.

[43] Ma, Y., S. Li, L. Zhang, S. Liu, Z. Liu, H. Li, and E. Shi, *Study on the effect of well layout schemes and fracture parameters on the heat extraction performance of enhanced geothermal system in fractured reservoir.* Energy, 2020. **202**: p. 117811.

[44] Shi, Y., X.Z. Song, J.C. Li, G.S. Wang, F.X. YuLong, and L.D. Geng, *Analysis for effects of complex fracture network geometries on heat extraction efficiency of a multilateral-well enhanced geothermal system.* Applied Thermal Engineering, 2019. **159**: p. 113828.

[45] Bahr, J., *" Modeling Density-Driven Flow in Porous Media".* Ground Water, 1999. **37**(4): p. 488-488.

[46] LI, X.-x., D.-q. LI, and Y. XU, *Equivalent simulation method of three-dimensional seepage and heat transfer coupling in fractured rock mass of geothermal-borehole system.* Engineering Mechanics, 2019. **36**(7): p. 238-247.

[47] Zheng, J., P. Li, B. Dou, T. Fan, H. Tian, and X. Lai, *Impact research of well layout schemes and fracture parameters on heat production performance of enhanced geothermal system considering water cooling effect.* Energy, 2022. **255**: p. 124496.

[48] Guo, T., S. Tang, J. Sun, F. Gong, X. Liu, Z. Qu, and W. Zhang, *A coupled thermal-hydraulic-mechanical modeling and evaluation of geothermal extraction in the enhanced geothermal system based on analytic hierarchy process and fuzzy comprehensive evaluation.* Applied Energy, 2020. **258**: p. 113981.

[49] Li, X.X., C.Y. Li, W.P. Gong, Y.J. Zhang, and J.C. Wang, *Probabilistic analysis of heat extraction performance in enhanced geothermal system based on a DFN-based modeling scheme.* Energy, 2023. **263**: p. 125674.

[50] Saeid, S., R. Al-Khoury, and F. Barends, *An efficient computational model for deep low-enthalpy geothermal systems.* Computers & Geosciences, 2013. **51**: p. 400-409.

[51] Huang, X., J. Zhu, J. Li, C. Lan, and X. Jin, *Parametric study of an enhanced geothermal system based on thermo-hydro-mechanical modeling of a prospective site in Songliao Basin.* Applied Thermal Engineering, 2016. **105**: p. 1-7.

[52] Miller, S.A., *Modeling enhanced geothermal systems and the essential nature of large-scale changes in permeability at the onset of slip.* Crustal Permeability, 2012: p. 353-362.

[53] Shi, Y., X. Song, J. Li, G. Wang, R. Zheng, and F. YuLong, *Numerical investigation on heat extraction performance of a multilateral-well enhanced geothermal system with a discrete fracture network.* Fuel, 2019. **244**: p. 207-226.

[54] Lauwerier, H.A., *The transport of heat in an oil layer caused by the injection of hot fluid.* Applied Scientific Research, Section A, 1955. **5**(2): p. 145-150.

[55] Barends, F. *Complete solution for transient heat transport in porous media, following Lauwerier's concept*. SPE Annual Technical Conference and Exhibition, 2010. SPE-134670-

MS.

[56] Song, X.Z., Y. Shi, G.S. Li, R.Y. Yang, G.S. Wang, R. Zheng, J.C. Li, and Z.H. Lyu, *Numerical simulation of heat extraction performance in enhanced geothermal system with multilateral wells.* Applied Energy, 2018. **218**: p. 325-337.

[57] Ma, Y.Y., S.B. Li, L.G. Zhang, S.Z. Liu, Z.Y. Liu, H. Li, E.X. Shi, and H.J. Zhang, *Numerical simulation study on the heat extraction performance of multi-well injection enhanced geothermal system.* Renewable Energy, 2020. **151**: p. 782-795.

[58] BAI, B., *One-dimensional thermal consolidation characteristics of geotechnical media under non-isothermal condition.* Engineering Mechanics, 2005. **22**(5): p. 186-191.

[59] Sun, Z.-x., X. Zhang, Y. Xu, J. Yao, H.-x. Wang, S. Lv, Z.-l. Sun, Y. Huang, M.-y. Cai, and X. Huang, *Numerical simulation of the heat extraction in EGS with thermal-hydraulic-mechanical coupling method based on discrete fractures model.* Energy, 2017. **120**: p. 20-33.

[60] Shi, Y., X.Z. Song, G.S. Wang, J.C. Li, L.D. Geng, and X.J. Li, *Numerical study on heat extraction performance of a multilateral-well enhanced geothermal system considering complex hydraulic and natural fractures.* Renewable Energy, 2019. **141**: p. 950-963.

[61] Zhang, Q. and A.D. Taleghani, *Autonomous fracture flow tunning to enhance efficiency of fractured geothermal systems.* Energy, 2023. **281**: p. 128163.

[62] Yi, Y. and E. Tawerghi, *Geometric percolation thresholds of interpenetrating plates in three-dimensional space.* Physical Review E—Statistical, Nonlinear, and Soft Matter Physics, 2009. **79**(4): p. 041134.